applied sciences

MDPI

Article

A Numerical Evaluation of Multi-Tine Electrode Geometry and Monopolar and Bipolar Operating Modes on the Efficacy of Radiofrequency Ablation in a Hepatic Tumor Model

Martyna Golebiowska [1], Arkadiusz Miaskowski [1,*] and Piotr Gas [2,*]

[1] Department of Electrical Engineering and Computer Science, Lublin University of Technology, 38D Nadbystrzycka Street, 20-618 Lublin, Poland; s98030@pollub.edu.pl
[2] Department of Electrical and Power Engineering, Faculty of Electrical Engineering, Automatics, Computer Science and Biomedical Engineering, AGH University of Krakow, Mickiewicza 30 Avenue, 30-059 Krakow, Poland
* Correspondence: a.miaskowski@pollub.pl (A.M.); piotr.gas@agh.edu.pl (P.G.)

Abstract

This study presents a comprehensive computational evaluation of radiofrequency (RF) ablation efficacy and the spatial formation of thermal ablation zones within a 3D model of a liver tumor. By systematically comparing these configurations, the study aims to elucidate the physical mechanisms governing electromagnetic (EM) energy dissipation in hepatic tissue and to provide clear engineering guidelines for optimizing RF applicator selection and treatment planning in clinical practice. To reliably simulate the biophysical phenomena of the RF ablation procedure, a coupled electro-thermal model based on the finite element method and the Pennes bioheat equation was implemented. The research investigates six distinct applicator variants: conventional needle-type applicators and advanced expandable umbrella-type RF applicators equipped with four- and eight-tine electrodes, each evaluated in both monopolar and bipolar configurations. Numerical simulations were conducted for a standard 10 min ablation procedure at varying applied voltages to assess the specific absorption rate (SAR) distribution, transient heating dynamics, and the exact volumes of the resulting coagulation necrosis which were quantified using rigorous isotherms and the cumulative equivalent minutes at 43 °C (CEM_{43}) thermal dose index. Volumetric analysis of the ablation zones revealed that bipolar multi-tine electrodes induce highly localized heat concentration. Conversely, monopolar multi-tine setups strongly disperse EM energy. The results demonstrated that, for conventional needle applicators, the monopolar configuration generated significantly larger necrosis zones than the bipolar operating mode. The RF applicator geometry and its operating mode directly dictate the spatial extent of liver tissue necrosis. Moreover, advanced numerical treatment planning is essential for optimizing SAR and CEM_{43} distributions and ensuring safe and complete hepatocellular carcinoma eradication.

Keywords: RF ablation; computational modeling; hepatocellular carcinoma; umbrella-type electrodes; monopolar and bipolar modes; SAR; CEM43; ablation zones

Check for updates

Academic Editors: Iman Farhat and Lourdes Farrugia

Received: 12 May 2026
Revised: 6 June 2026
Accepted: 9 June 2026
Published: 12 June 2026

Copyright: © 2026 by the authors. Licensee MDPI, Basel, Switzerland. This article is an open access article distributed under the terms and conditions of the Creative Commons Attribution (CC BY) license.

1. Introduction

Primary and metastatic liver malignances, including hepatocellular carcinoma, represent a major clinical challenge in modern medicine [1]. When surgical resection of a

liver tumor is impossible or too risky for the patient, modern minimally invasive therapeutic methods are used, among which radiofrequency ablation (RFA) and microwave ablation (MVA) play a pivotal role [2]. These procedures enable targeted destruction of tumors located deep within the human body, thereby reducing procedural invasiveness and improving patient safety [3]. Moreover, ablative therapies have demonstrated high efficacy not only in hepatic tissue but also in the treatment of malignancies affecting other organs [4], such as breast [5], lung [6] and prostate cancers [7,8].

The RFA procedure involves the percutaneous insertion of specialized applicators equipped with various active electrode configurations directly into the center of the tumor that generate an EM field [9]. To make ablation techniques more precise and safer, the positioning of applicators in the target tissue is performed using robot-assisted interventions and image-guided interventions [10]. The RF electric field generated by alternating electric current with a frequency in the range of 450–550 kHz induces rapid ionic motion in the tissue, causing local heat generation due to ohmic losses, commonly referred to as Joule heating [11,12]. When tissue temperature exceeds critical physiological thresholds, irreversible destruction of cancer cells occurs, referred to as coagulation necrosis [13]. The efficacy of cellular destruction is typically evaluated by checking whether the tissue has reached a rigorous, destructive temperature (above 50 °C) [14], or by using the thermal dose indices of Arrhenius thermal tissue damage [15,16] and cumulative equivalent minutes at 43 °C (CEM43) [17–19]. Accurate prediction of these outcomes depends heavily on computational modeling of temperature-controlled ablation processes [20–23].

The primary challenge in RFA therapy is to destroy the entire tumor along with an adequate safety margin, while simultaneously avoiding damage to the healthy surrounding tissues. This is a very difficult task because the blood flowing through the surrounding organs, as well as blood vessels within the tumor, constantly cool the cancerous tissue (the so-called heat sink effect), as a result of which the peripheral regions of large tumors may not be sufficiently heated [20,24–27]. For this reason, biomedical engineers are constantly developing new applicator designs for localized cancer treatment [9,28–31]. Conventional needle electrodes are systematically being replaced by multi-tine expandable umbrella-type electrodes, which incorporate deployable tines, allowing a significant increase in the active heating area within the tumor [9,16,20,32]. Additionally, the operating mode has a profound influence on the shape of the ablation zone, i.e., in monopolar mode the current flows to external grounding pads on the patient's body, whereas in bipolar mode, the current is completed locally between the poles on the electrode itself [9,33,34].

Considering the wide range of RF applicator designs and electrode operating modes, it becomes evident that in vivo studies are very costly and difficult to conduct compared to in silico investigations based on computational modeling, which has become the standard tool for treatment planning and testing of ablative procedures [14,35]. Numerical simulations employ various approaches, particularly the finite element method (FEM), which enables coupling electromagnetic (EM) field calculations with the modified Pennes bioheat equation [24,36–40]. Using such numerical methods, it is possible to accurately predict the specific absorption rate (SAR) distribution and generate 3D temperature distributions within patient-specific models prior to the clinical procedure [14,35].

The aim of this study is to computationally evaluate RF ablation efficacy and the spatial formation of necrotic zones in a 3D model of a liver tumor. The study compares six different applicators: conventional needle-type electrodes and advanced expandable umbrella-type electrodes equipped with four and eight tines, operating in both monopolar and bipolar modes. The analysis includes the impact of electrode geometry and operating mode on the SAR distribution, tumor thermal dynamics, and ablation zone volume, with

the objective of providing clear engineering guidelines for improving RF ablation treatment planning of hepatocellular carcinoma.

2. Materials and Methods

This section describes the complete mathematical approach, based on the coupled electromagnetic (generalized Laplace equation) and thermal (modified Pennes equation) models, required for the computational simulation of RF ablation in hepatic tumor tissue.

2.1. Computational Model

Numerical calculations were performed using the Sim4Life Lite software environment (version 9.4.0) [41,42], utilizing a multiphysics solver based on the finite element method (FEM) engine. The analysis was conducted in two stages, in accordance with the well-established multi-step approach in computational bioelectromagnetism [14,19,35]. In the first stage, the EM field distribution, governed by the generalized Laplace equation, was determined using the ohmic Electro-Quasi-Static (E-QS) solver. In the second stage, the transient temperature distribution was calculated using a Thermal Solver (TS) based on the modified Pennes bioheat equation. The volumetric power density calculated in the EM stage served directly as the heat source (p) for the thermal stage as shown in Equations (4) and (5).

Within the E-QS regime, the lack of external electric current sources allows the magnetic vector potential to be neglected. Consequently, the resulting electric field is strictly governed by the gradient of the scalar electric potential ϕ. The continuity of this potential at the domain boundaries is guaranteed by the generalized Laplace equation for the electro-quasi-static model as [23,43–45]:

$$\nabla \cdot (\underline{\varepsilon}\, \nabla \phi) = 0 \tag{1}$$

where $\underline{\varepsilon} = \varepsilon_r\, \varepsilon_0 + \sigma/(j\omega)$ represents the complex electric permittivity of the medium, ε_r stands for the relative electric permittivity, $\varepsilon_0 = 8.85 \times 10^{-12}$ F/m is the electric constant, σ (S/m) is the effective electrical conductivity of the tissue, j means the imaginary unit ($j^2 = -1$), and $\omega = 2\pi f$ (rad/s) represents the angular frequency of the EM field with operating frequency f (Hz).

Accordingly, the vector of electric field strength $\mathbf{E}$ (V/m) can be defined as the negative gradient of the scalar potential [14]:

$$\mathbf{E} = -\nabla \phi \tag{2}$$

Next, the EM energy (the volumetric power density p in W/m^3) deposited within biological tissues due to dielectric losses can be calculated directly from the computed electric field distribution and expressed in terms of the SAR parameter [35,46]:

$$p = \sigma\, |\, \mathbf{E}_{RMS}\, |^2 = \sigma\, |\, \nabla \phi\, |^2 = \rho\, \mathrm{SAR} \tag{3}$$

where ρ (kg/m^3) is the mass density of the tissue, and $|\, \mathbf{E}_{RMS}\, |$ and ϕ denote the root-mean-square (RMS) values of the electric field and the electric potential, respectively. To close the problem formulation for the E-QS solver, boundary conditions of the first kind (the so-called Dirichlet boundary conditions) may be imposed on the active surfaces of the electrodes (see Figure 1a).

In the subsequent simulation part, the previously calculated distribution of power loss density p (W/m^3) becomes a spatial heat source in the transient thermal solver. The

temporal changes in temperature T (K) changes over time t (s) can be modeled using the widely recognized, modified Pennes equation as follows [24,46]:

$$\rho c \frac{\partial T}{\partial t} = \nabla \cdot (\kappa \nabla T) \; - \rho_b c_b \omega_b (T - T_b) \; + \rho \mathrm{HGR} + p \tag{4}$$

In the above relation, c (J/kg/K) denotes the specific heat capacity, κ (W/m/K) means the thermal conductivity coefficient, and ω_b (1/s) defines the perfusion rate of blood flowing through the tissue. The subscript b characterizes the properties of the flowing blood, i.e., ρ_b is the blood density, T_b means the arterial blood temperature, and c_b stands for the blood heat capacity. In turn, the heat generation rate (HGR in W/kg) reflects the amount of heat produced locally through the metabolic processes inside biological tissues. It should be noted that the Pennes equation as used in Equation (4) omitted the latent heat of the water vaporization effect as described in [47]. Such a simplified approach has been successfully adopted in numerous in silico investigations [20,35].

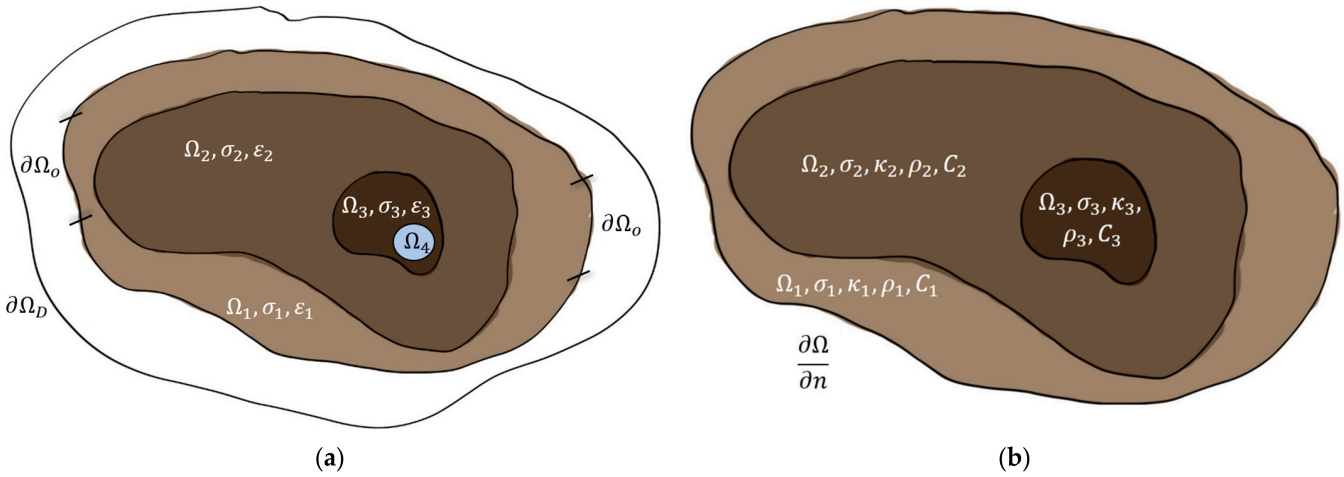


Figure 1. Computational model with marked boundary conditions: (**a**) Electro-Quasi-Static (E-QS) solver—Dirichlet boundary condition $\partial\Omega_D$ set on the outer domain boundary, electrical parameters (σ, ε) defined in subdomains Ω_1–Ω_4; (**b**) Thermal Solver (TS)—Neumann boundary condition $\partial\Omega/\partial n$ applied the outer domain boundary, thermal parameters (κ, ρ, c) defined in subdomains Ω_1–Ω_3.

Furthermore, to isolate the model from artificial energy losses at the outer boundaries of the computational domain, the boundary condition of the second kind, well known as the Neumann boundary condition, was applied, implying ideal thermal insulation at the external boundaries was enforced [19] (see Figure 1b).

The computational domain consists of four subdomains: Ω_1—phantom; Ω_2—healthy liver tissue; Ω_3—hepatic tumor; and Ω_4—the RF applicator represented by voltage electrodes with assigned electric potential ϕ. 3D models of the ablation electrodes were designed in the CAD software Autodesk Inventor 2025 (Autodesk Inc., San Rafael, CA, USA) and then imported to the Sim4Life Lite environment [41]. The hepatic tumor geometry was modeled as an irregular ellipsoidal structure with a volume of V_{tumor} = 1941.2 mm^3, as such a shape provides a realistic representation of naturally occurring tumors [35].

Appropriate boundary conditions were defined for both simulation steps as shown in Figure 1. In the E-QS problem, based on Equation (1), two cases were considered, i.e., applicators in monopolar and bipolar modes. For the monopolar mode, the Dirichlet boundary conditions were applied to the outer boundaries of the domain $\partial\Omega_D$, whereas a non-zero electric potential ($\phi \neq 0$) was assigned to subdomain Ω_4, and a part of the subdomain Ω_1 was grounded ($\partial\Omega_0 = \phi = 0$). In the case of the bipolar mode, to represent the electrodes, the condition $\partial\Omega_0 = 0$ on Ω_1 was omitted, but Ω_4 was divided into two parts

separated by an insulator, i.e., one part with non-zero potential ($\phi \neq 0$) and the other part with zero potential ($\phi = 0$).

In the thermal problem, based on Equation (4), the Neumann boundary condition $\partial\Omega/\partial n = 0$ was assigned to the outer boundaries of the domain Ω_1. The initial temperature throughout the domain was set to $T(t = 0) = T_0$, and the blood temperature of tissue was kept constant at $T(t \neq 0) = T_b$ throughout the simulation [14,19].

The computational domain was modeled as an isotropic block of healthy liver tissue with a total volume of approximately 1.56×10^6 mm^3 and overall dimensions of $115.9 \times 115.9 \times 115.9$ mm. A tumor model in the shape of a flattened ellipsoid was embedded in its central part, characterized by an initial volume of 1941.2 mm^3 and a surface area of 857.7 mm^2. The spatial dimensions of the lesion under investigation, measuring $20 \times 20 \times 9.72$ mm, provide a realistic representation of the asymmetrical pathological structure undergoing virtual thermal ablation.

To optimize the computational process, all biological tissues and RF applicator components within the domain were treated as time-constant, isotropic, and homogeneous materials. This approach constitutes a standard and well-documented practice in the computational modeling of thermal therapies [35,48–51]. The specific values for the electrical and thermal properties of the analyzed tissues were adopted from the IT'IS Foundation Database [52]. The active surfaces of the electrodes were defined as perfect electric conductors (PECs), and the dielectric elements of the RF applicators were modeled as polyethylene.

To evaluate thermally induced tumor cell destruction, the iso-effective dose metric was employed [53]. In radiology, hyperthermia and ablation treatments, the standard metric for assessing thermal dose of tissues is the index of cumulative equivalent minutes at 43 °C (CEM_{43}) [17,54–56]. This metric integrates the cumulative thermal dose absorbed by the tissue over the duration of the treatment procedure, based on the following formula [17,19,53–56]:

$$CEM_{43} = \int_0^t R^{43-T(t)} dt \quad (5)$$

where the parameter R serves as an empirical constant that responds nonlinearly to specific temperature thresholds. Based on the original Sapareto and Dewey formulation [56], $R = 0.5$ for $T \geq 43$ °C, and $R = 0.25$ for $T < 43$ °C [19,53–56].

2.2. Ablation Electrode Models

To reflect the designs of applicators such as those used in clinical thermal ablation of soft tumor tissues [57], six representative RF electrode configurations were investigated, as shown in Figure 2. The investigated RF electrode systems comprise both monopolar and bipolar needle-type RF applicators, as well as monopolar and bipolar umbrella-type RF applicators with expandable multi-tine electrodes with 4 and 8 arms. The monopolar applicator (Figure 3a) comprises an insulated shaft and an exposed, electrically conductive distal tip (electrode 1). In the bipolar mode electrode variant (Figure 3b,c), an additional active conductive section (Electrode 2) is located on the same shaft, separated from electrode 1 by a dielectric (insulator).

In the monopolar configuration (Figure 3a), electric current flows between the active electrode tip and two large-surface grounding pads (neutral plates) placed on the patient's body. In the bipolar configuration, both poles (anode and cathode) are integrated into a common applicator shaft, which confines the electric current flow to the immediate vicinity of the tumor and eliminates the need for passive electrodes [9]. Expandable electrodes feature umbrella-shaped tines deployed from the needle lumen. This design significantly increases the effective contact area at the electrode–tissue interface, enabling the creation of larger ablation zones while reducing the local current density near the shaft [9].

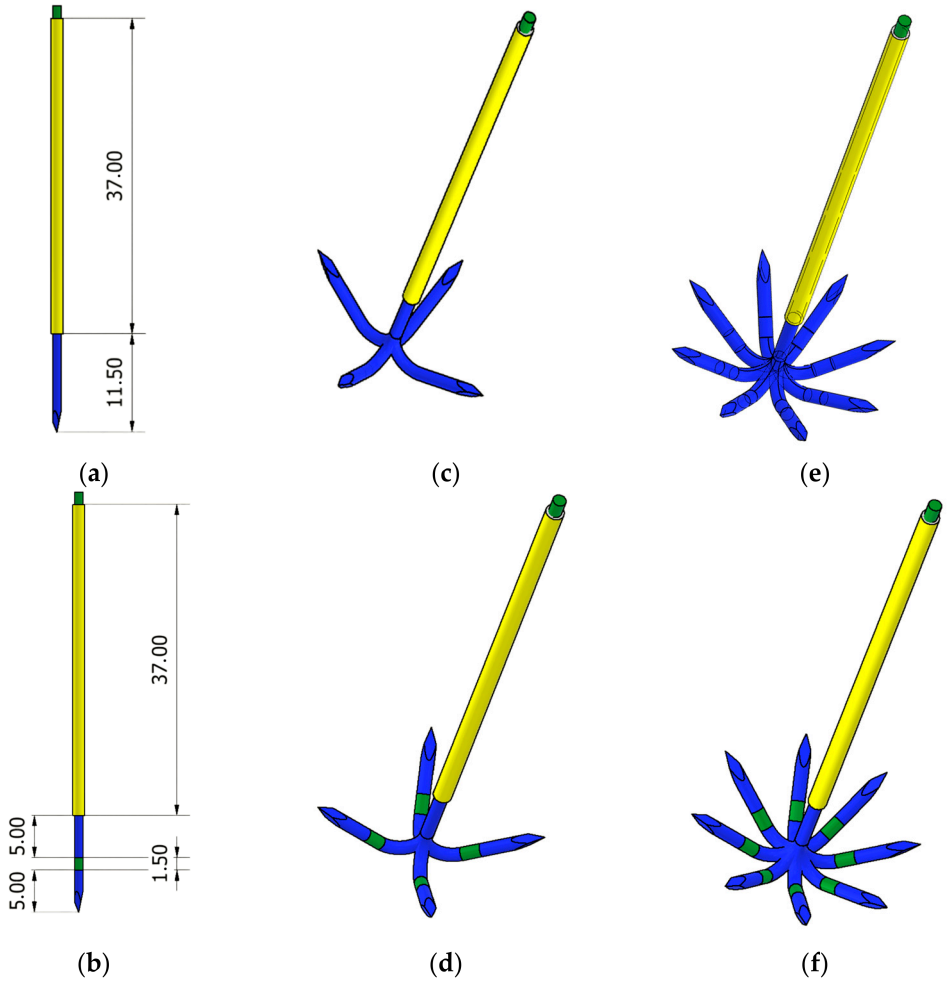


Figure 2. Geometric models of the analyzed RF applicators used for ablation treatment: (**a**) monopolar needle-type applicator; (**b**) bipolar needle-type applicator; (**c**) monopolar expandable 4-tine umbrella-type applicator; (**d**) bipolar expandable 4-tine umbrella-type applicator; (**e**) monopolar expandable 8-tine umbrella-type applicator; (**f**) bipolar expandable 8-tine umbrella-type applicator (all dimensions are in mm).

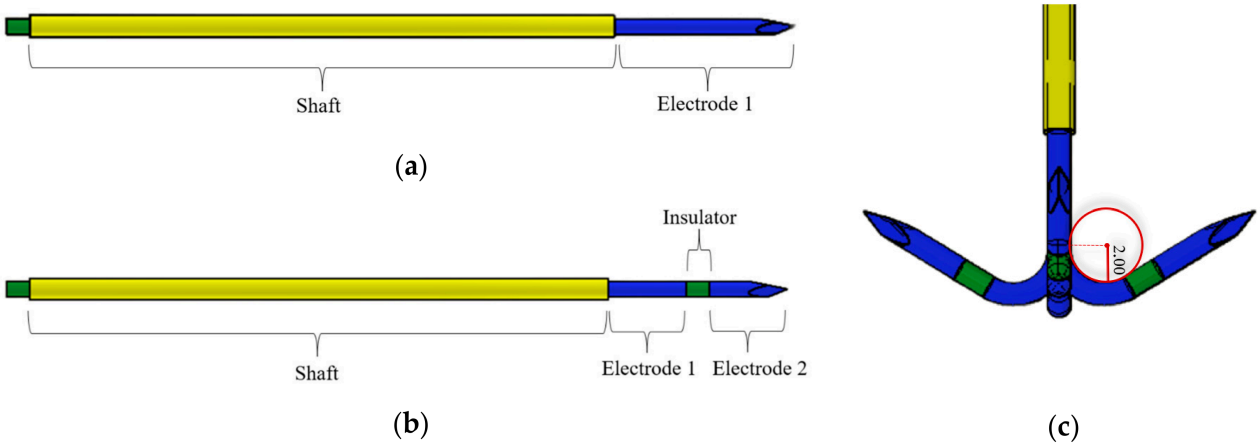


Figure 3. A schematic diagram of the classic needle-type (plain) RF applicators used in the simulation: (**a**) a monopolar applicator with a single active tip; (**b**) a bipolar applicator featuring distal and proximal active sections separated by a dielectric insulator; (**c**) a bipolar expandable multi-tine applicator (all dimensions are in mm).

The geometries of the designed RF electrode models correspond to those of commercially available RF applicators for ablation treatment [18]. A detailed summary of the geometric parameters for all six analyzed electrode configurations is gathered in Table 1.

Table 1. The geometric dimensions of the six configurations of RF applicators used in the simulation.

Applicator Elements	RF Applicator Types					
	Monopolar	Bipolar	Monopolar 4-Tine Electrode	Bipolar 4-Tine Electrode	Monopolar 8-Tine Electrode	Bipolar 8-Tine Electrode
Radius of the shaft (mm)	0.7	0.7	0.7	0.7	0.7	0.7
Radius of the insulator (mm)	0.5	0.5	0.5	0.5	0.5	0.5
Radius of the electrodes (mm)	0.5	0.5	0.5	0.5	0.5	0.5
Length of the shaft (mm)	37.0	37.0	37.0	37.0	37.0	37.0
Length of the insulator (mm)	–	1.5	–	1.5	–	1.5
Length of the electrode 1 (mm)	–	5.0	–	5.0	–	5.0
Length of the electrodes 2 (mm)	11.5	5.0	11.1	5.0	11.1	5.0
Length of expandable tines (mm)	–	–	3.5	3.5	3.5	3.5
Tines opening angle (°)	–	–	122.9	122.9	122.9	122.9
Inter-tine angle (°)	–	–	90.0	90.0	45.0	45.0

All proposed RF applicators were assumed to operate at a frequency of 500 kHz, which is a typical operating frequency for ablation procedures.

2.3. Material Parameters of Biological Tissues

The thermal and electrical properties assigned to the subdomains of the liver tissue phantom were taken from the IT'IS Database for Thermal and Electromagnetic Parameters of Biological Tissues (version 5.0) [52]. These parameters are a widely recognized standard in computational bioelectromagnetics and are in good agreement with experimentally measured properties of human tissues and the literature data on numerical modeling of RF ablation [35,58]. The dielectric properties of materials implemented in the EQ-S solver for the working frequency of 500 kHz are provided in Table 2. The electrodes were modeled as perfect electric conductors (PECs). The thermal parameters of biological tissues implemented in the thermal solver are summarized in Table 3.

Table 2. The dielectric parameters of the materials used in the simulation at frequency of 500 kHz [14,52].

Materials	ε_r (–)	σ (mS/m)
liver tissue	2769	148
liver tumor	3647	446
insulator	2.25	0.5
electrodes	–	–

Table 3. The thermal parameters of the biological tissues used in the simulation [52].

Tissues	ρ (kg/m^3)	c (J/kg/K)	κ (W/m/K)	HGR * (W/kg)	$\rho_b c_b \omega_b$ (kW/m^3/K)	ω_b (1/s)
blood	1050	3617	0.520	0	664.6	0.1750
liver tissue	1079	3540	0.519	9.93	62.7	0.0165
liver tumor	1040	3437	0.560	12.0	51.0	0.0134

* Heat generation rate.

The tumor tissue was modeled based on the properties of muscle tissue, which is a literature-supported approach for liver tumors [14]. Hepatocellular carcinoma (HCC) has a significantly higher water content and better blood supply than healthy liver tissue. For this reason, its electrical conductivity is markedly higher. To model this in the simulation, the dielectric properties of muscle tissue were used. Muscle tissue exhibits comparable hydration levels and electrical conductivity. This approach provides a proven surrogate model that enables reliable simulation of increased RF energy absorption within the tumor. The naturally higher value of the electrical conductivity of the tumor (σ = 0.446 S/m) relative to healthy liver tissue (σ = 0.148 S/m) promotes preferential concentration of the electric field strength (**E**) and electric current density (**J** = σ **E**) within the cancer lesion, thereby increasing the selectivity of thermal destruction of the malignant hepatic tissue [14]. The heat generation rate (HGR) for blood was set to zero, since convection (perfusion) rather than local metabolic heat generation of the tissue dominate blood heat transfer.

2.4. RF Applicators Parameters

To comprehensively evaluate the thermal response and ablation treatment efficacy of the investigated RF applicators, a series of systematic numerical simulations was conducted under predefined operating conditions. The continuous-wave RF radiation was simulated at a fundamental frequency of 500 kHz, which is representative of standard clinical RF generators [9,57].

To simulate varying RF energy outputs and assess the spatial progression of the ablation zones, four electric potential levels were applied to the active electrode surfaces, namely $\phi \in \{10, 15, 20, 25\}$ V. In monopolar RF applicators, these potentials were assigned directly to the distal active tip. In bipolar configurations, the excitation voltage was applied to the designated active pole, with the corresponding complementary electrode grounded (ϕ = 0 V) to facilitate local electric current flow.

The transient thermal solver was configured to compute the spatiotemporal evolution of the tissue temperature over a total continuous exposure duration of 600 s. This exposure duration accurately reflects standard clinical ablation protocols and ensures sufficient thermal dose accumulation [14,19,35]. As previously established in the boundary condition definitions, the baseline physiological temperature for the entire computational domain prior to RF energy delivery was uniformly initialized at T_0 = 37 °C. Furthermore, the thermoregulatory influence of vascular blood perfusion was incorporated by maintaining the arterial blood temperature T_b = 37 °C throughout the entire heating process.

3. Results

This section presents and discusses the results for the coupled electro-thermal problem, including the main observations regarding the electric field strength, specific absorption rate (SAR) and temperature distributions around the proposed monopolar and bipolar RF applicators.

The ohmic EQ-Static solver mesh was refined to 0.2 mm around the electrodes, to 0.5 mm within the tumor volume, and to 10 mm in healthy tissue, resulting in a total of 1.279 million cells (the convergence tolerance was set to 10^{-8}). In the case of the thermal solver, the mesh comprised approximately 536,000 cells (0.7 mm in the tumor, 2.5 mm in the liver). An adaptive time step algorithm (time step factor = 1) was used in the thermal calculations. Preliminary convergence tests (global mesh refinement using a factor of 1.5) showed changes in maximum SAR and temperature values of less than 1%. These results confirmed asymptotic convergence, at which point further refinement of the mesh would only result in a significant increase in computation time without improving the accuracy of the results.

3.1. Spatial Distribution of the Electric Field Strength

The analysis of the electric field distribution was carried out based on the solution of the generalized Laplace Equation (1), which enabled the scalar potential ϕ to be determined throughout the entire volume of the computational model. Subsequently, in accordance with Equation (2), the distribution of vector of electric field strength, **E**, was calculated. The results shown in Figure 4 present the effective (RMS) values of vector **E** for the six tested configurations of RF applicators at the maximum applied electrode voltage of 25 V. The electric field (E-field) estimated in this manner forms the basis for further calculations of the SAR according to Equation (3).

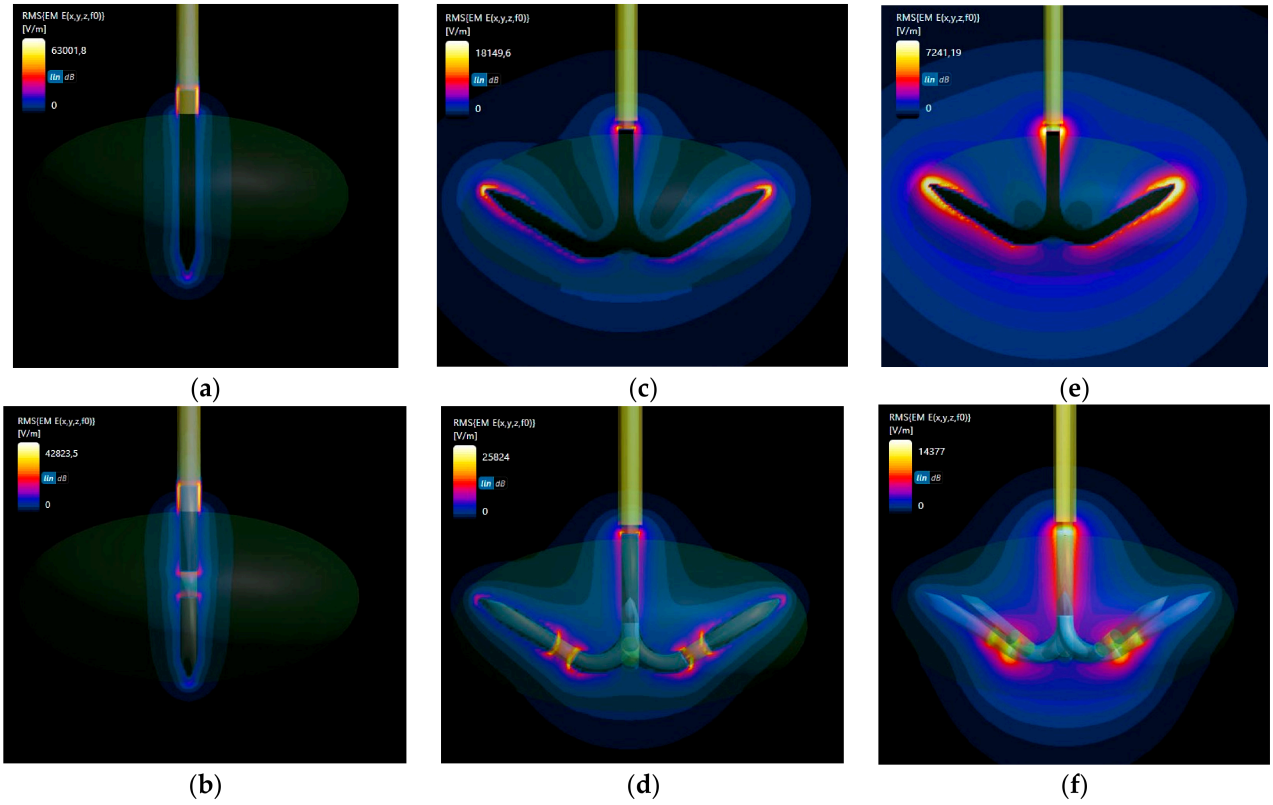


Figure 4. Axial cross-section spatial E-field distributions around various RF ablation applicator configurations: (**a**) monopolar needle-type applicator; (**b**) bipolar needle-type applicator; (**c**) monopolar expandable 4-tine umbrella-type applicator; (**d**) bipolar expandable 4-tine umbrella-type applicator; (**e**) monopolar expandable 8-tine umbrella-type applicator; (**f**) bipolar expandable 8-tine umbrella-type applicator; for applied electrode voltage of 25 V.

The highest values of electric field strength were observed for classic needle-type applicators. In the case of monopolar configuration (Figure 4a), the E-field was concentrated at the distal, sharp tip of the applicator, reaching a maximum value of 63 kV/m. In bipolar mode (Figure 4b), the E-field was confined to a short section within the dielectric gap of the insulator between the two active sections of the shaft, and its maximum value was 42.8 kV/m. In both cases, the zone of the strongest field was very narrow and limited to the immediate vicinity of the RF electrode surface, making them suitable for the treatment of small hepatic neoplastic lesions.

In the case of multi-tine applicators, the electric field covers a much larger volume of hepatic tissue, which causes a decrease in its maximum intensity. The bipolar expandable 4-tine umbrella-type applicator (Figure 4d) generated a maximum peak E-field value of 25.8 kV/m. Changing the operating mode to monopolar for the same electrode (Figure 4c) caused the E-field lines to disperse spatially toward the distant passive electrode, resulting

in a reduction in the maximum E-field intensity to 18.1 kV/m. A similar phenomenon was observed for umbrella-type electrodes equipped with eight arms. Bipolar mode (Figure 4f) causes a strong concentration of the electric field inside the applicator dome, reaching a maximum value of 14.4 kV/m. In contrast, the 8-tine monopolar mode electrode (Figure 4e) exhibited the widest spatial distribution of the E-field among all tested variants. The uniform distribution of RF field energy over the largest active surface resulted in the lowest recorded peak E-field intensity of 7.2 kV/m.

To conclude, multi-tine applicators provide a significantly wider distribution of electric field strength than conventional needle electrodes. However, this wider coverage is accompanied by a marked decrease in E-field intensity, which is particularly evident in monopolar electrode configurations. Consequently, for hepatic lesions, expandable umbrella-type applicator designs demonstrate a greater potential for more uniform EM energy delivery throughout the malignant tissue volume.

3.2. Spatial Distribution of the Specific Absorption Rate

Based on the spatial distribution of the electric field obtained in the previous step, the specific absorption rate (SAR) was calculated in accordance with Equation (3). Figure 5 shows visualizations of the spatial distribution of the SAR parameter on a logarithmic scale in dB (the maximum SAR was taken as the reference level) for all tested RF applicators with maximum electrode voltage of 25 V.

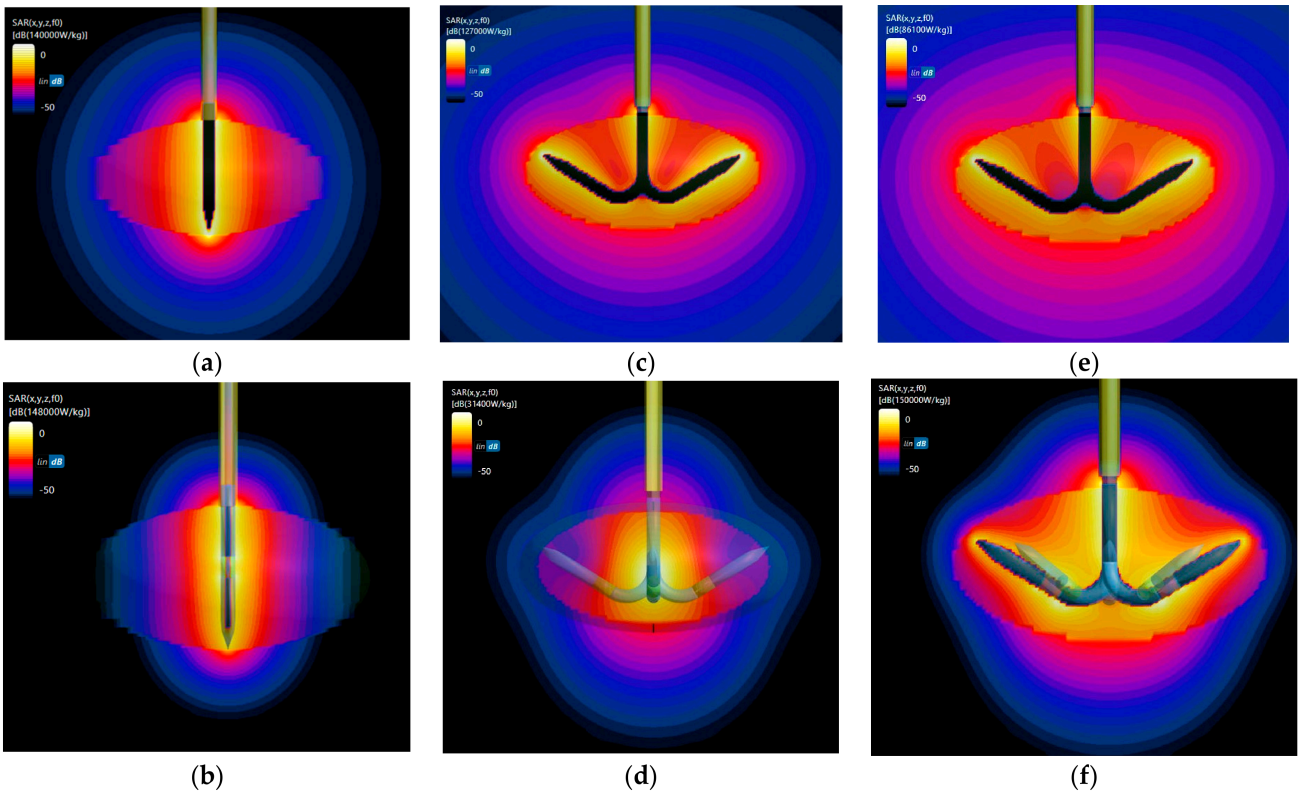


Figure 5. Axial cross-section SAR distributions inside the liver tumor tissue for various RF ablation applicator configurations: (**a**) monopolar needle-type applicator; (**b**) bipolar needle-type applicator; (**c**) monopolar expandable 4-tine umbrella-type applicator; (**d**) bipolar expandable 4-tine umbrella-type applicator; (**e**) monopolar expandable 8-tine umbrella-type applicator; (**f**) bipolar expandable 8-tine umbrella-type applicator; for applied electrode voltage of 25 V.

The results indicate that the most significant differences in the distribution of RF field energy deposition are particularly evident for multi-tine applicators. In the bipolar

configuration (for both four- and eight-tine applicators), the electric field lines close over a very short distance between the deployed tines and the common applicator shaft. This leads to an extreme concentration of SAR values within the portion of tumor tissue enclosed by the umbrella-type electrode. For the 4-tine bipolar applicator (Figure 5d), the peak SAR value reached 31.4 kW/kg, whereas for the 8-tine bipolar electrode design (Figure 5f), the SAR value increased to 150 kW/kg. This phenomenon of strong, local confinement of the RF field energy deposition constitutes the primary physical mechanism of the drastic temperature increments in tissue areas with the highest SAR values.

A completely different mechanism occurs in expandable umbrella-type applicators operating in the monopolar mode. In this case, the electric current flows from all deployed tines toward the distant passive electrode (grounding at the boundaries of the computational domain). This results in a significant spatial dispersion of the RF field energy deposited in the tissue. Consequently, the peak SAR values are altered. The 4-tine monopolar electrode configuration (Figure 5c) recorded a peak of 127 kW/kg, while the 8-tine monopolar applicator (Figure 5e) exhibited the strongest dispersion effect, reducing the maximum SAR value of 36.1 kW/kg. The region exhibiting the highest SAR values extends radially over a much larger volume of the tumor, which prevents extreme tissue overheating in the immediate vicinity of the RF applicator, thereby producing a milder yet more uniform liver heating profile.

For standard needle-type applicators, the SAR distributions reflect the thermal profiles. In the monopolar setup (Figure 5a), energy is deposited most strongly around the single distal tip, with a characteristic enhancement at the very point itself (resulting from the edge effect and a local increase in the electric potential gradient), achieving a SAR peak of 148 kW/kg. However, in the bipolar mode (Figure 5b), the maximum SAR value, reaching a level of 140 kW/kg, is concentrated in the dielectric gap separating the two active electrodes, forcing local heating along the RF applicator shaft.

The presented SAR analysis demonstrates that, in the case of multi-tine electrodes, the bipolar operating mode confines energy within the electrode tip, causing extreme, localized heating. In contrast, the monopolar mode disperses EM energy widely, preventing excessive local tissue overheating and heating a larger volume evenly. Therefore, the choice of RF applicator geometry and proper operating mode directly determines whether the ablation procedure will act as a strong focal point or over a wider area of treated tissue.

3.3. Analysis of Temperature Distribution

A non-stationary thermal solver was used to analyze the temperature distribution inside liver tissue according to Equation (4). The spatial SAR distributions obtained in the previous step were incorporated in the Pennes bioheat equation as a volumetric heat source, given by Equation (5), which influences the tumor temperature. Such a coupled electro-thermal approach allowed time-dependent tissue-heating dynamics to be modeled, whilst taking into account the physiological cooling process induced by blood perfusion.

Figures 6–8 present the hepatic tumor transient temperature profiles recorded over a 10 min simulation at four levels of applied electrode voltage $U \in \{10,15,20,25\}$ V. The results are compared both for the monopolar (dashed lines) and bipolar (solid lines) electrode configurations.

As illustrated in Figure 6, both operating mode (monopolar and bipolar) configurations exhibit similar heating dynamics. The temperature rise is steepest during the first 100 s of the RF ablation procedure. The highest steady-state temperatures of approximately 81 °C were observed for the bipolar applicator and 85 °C for the monopolar applicator, respectively, at an applied electrode voltage of 25 V. In this case, the monopolar mode demonstrated slightly higher local heating efficacy, which results from the strong concen-

tration of electric current density at the single distal active electrode tip, where the E-field radiates outward into the liver tissue.

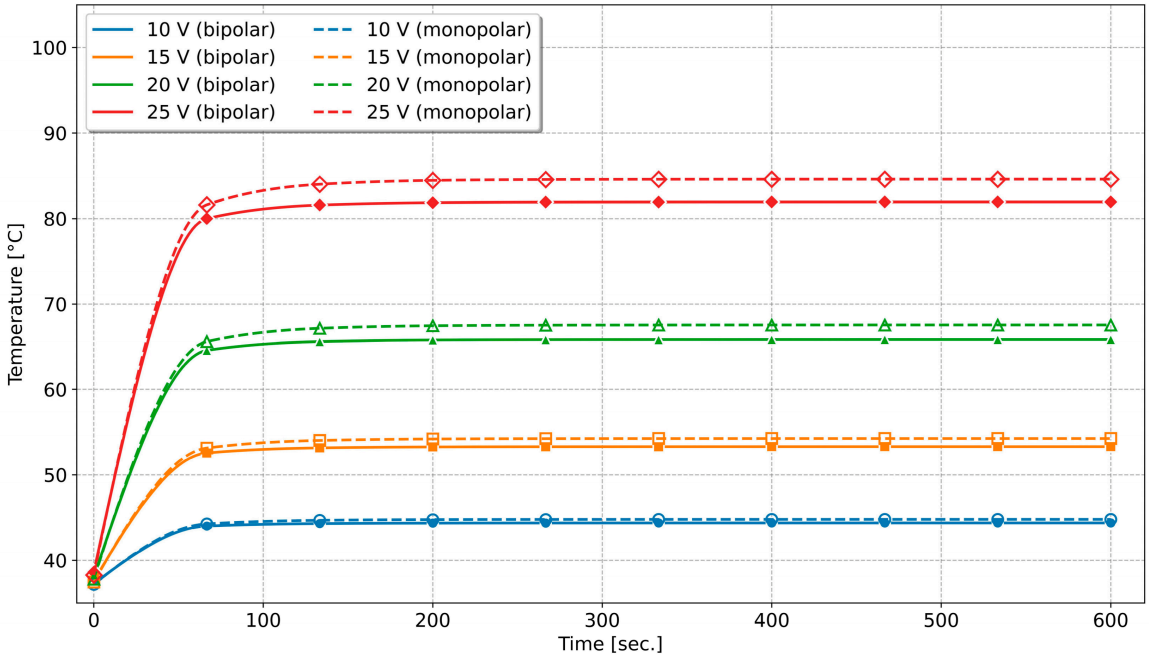


Figure 6. The hepatic tumor transient temperature distribution for classic needle-type applicators in the case of monopolar and bipolar configurations for different values of applied electrode voltage (the hottest voxel, located at the active electrode–tissue interface).

In contrast, the bipolar configuration distributes the electric field more evenly between the two closely spaced poles, mitigating focal current spikes. Consequently, while the bipolar mode yields a slightly lower maximum temperature, it promotes a more uniform thermal profile and reduces the risk of tissue carbonization directly at the electrode surface.

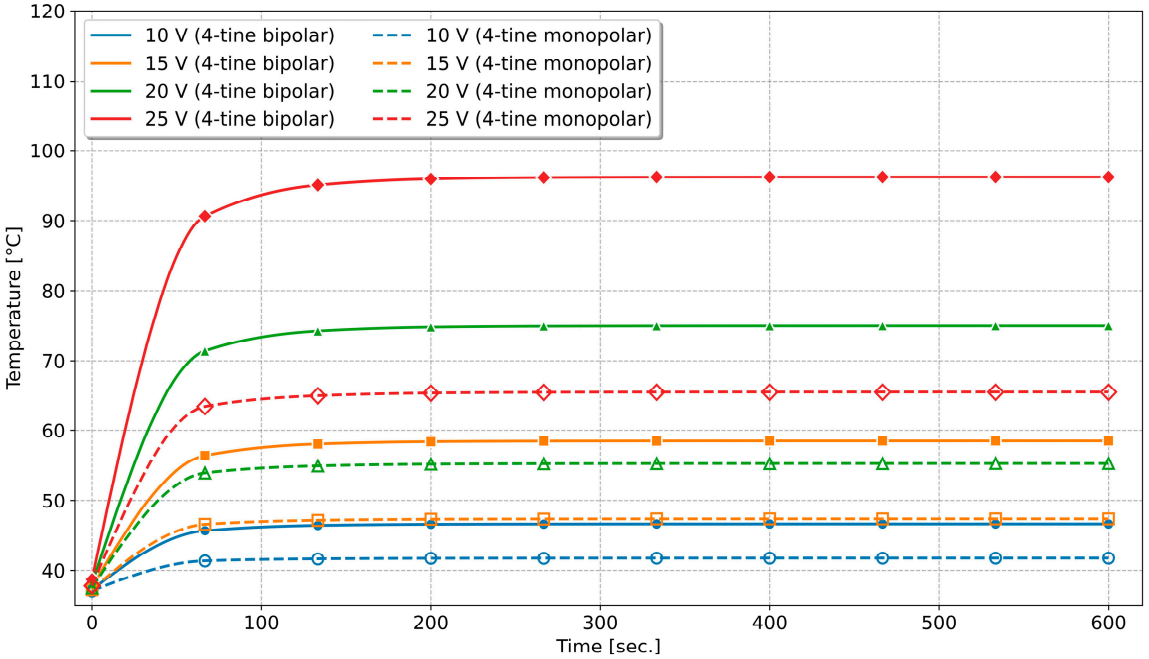


Figure 7. The hepatic tumor transient temperature distribution for 4-tine umbrella-type applicators in the case of monopolar and bipolar configurations for different values of applied electrode voltage (the hottest voxel, located at the active electrode–tissue interface).

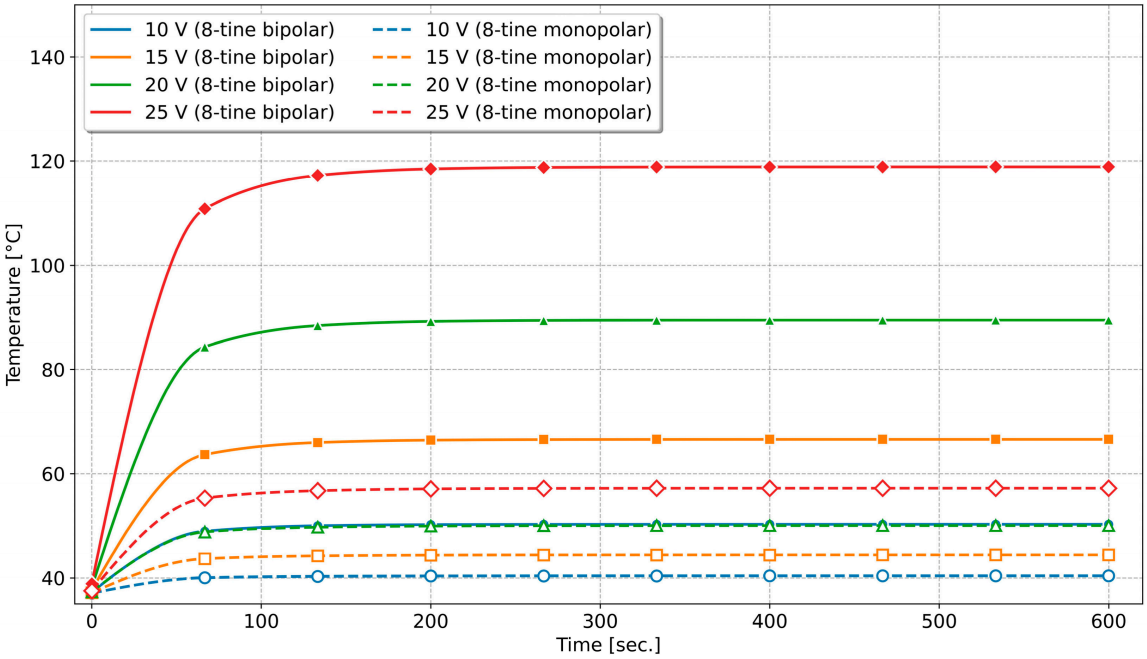


Figure 8. The hepatic tumor transient temperature distribution for 8-tine umbrella-type applicators in the case of monopolar and bipolar configurations for different values of applied electrode voltage (the hottest voxel, located at the active electrode–tissue interface).

Radical differences between the monopolar and bipolar modes become apparent in the case of expandable multi-tine applicators. As shown in Figure 7, a 4-tine applicator with bipolar mode configuration generates significantly higher maximum temperatures than the corresponding monopolar configuration for each of the analyzed electrode voltages. At an applied voltage of 25 V, the bipolar applicator heated the liver tissue to 96 °C, while the monopolar applicator reached a temperature of only 65 °C.

This phenomenon is further amplified when the number of tines in the umbrella-type electrode is increased to eight (see Figure 8). The application of an electrode voltage of 25 V in the 8-tine bipolar applicator resulted in an extremely high temperature of 119 °C. This is due to the fact that in bipolar mode, the electric current is locally confined over a very short distance between the deployed tines and the electrode shaft, leading to a drastic concentration of the electric field in the immediate vicinity of the RF applicator. A temperature approaching 120 °C is associated with the risk of carbonization of healthy tissue under clinical conditions.

In the monopolar mode, increasing the number of electrode tines from four to eight caused a slight decrease in the maximum level of steady-state temperature (from 65 °C to 57 °C at 25 V). Distribution of the active surface area over a larger number of tines results in the dispersion of the total electric current density flowing toward the distant passive electrode, which reduces the local Joule heating effect but also allows for more uniform heating of a larger liver tumor tissue volume.

To precisely quantify the observed thermal phenomena, Table 4 summarizes the total temperature increments ΔT recorded in the tissue after a 10 min ablation procedure for all six analyzed RF applicator variants. The ΔT value was calculated as the difference between the maximum steady-state temperature and the initial physiological human body temperature (37 °C). An analysis of the tabular data corroborates the observations derived from the tissue transient temperature and highlights key physical relationships regarding the operating modes and electrode geometry of the RF applicators.

Table 4. The total temperature increments ΔT (°C) in the liver tumor center after 10 min of ablation treatment for the investigated applicator configurations and applied RF electrode voltage levels.

Electrode Voltage U (V)	Total Temperature Increments ΔT (°C)					
	Needle-Type Applicator		4-Tine Umbrella-Type Applicator		8-Tine Umbrella-Type Applicator	
	Monopolar	Bipolar	Monopolar	Bipolar	Monopolar	Bipolar
10	7.11	7.58	9.39	4.59	12.98	3.31
15	15.73	16.80	20.85	10.08	28.93	7.21
20	27.80	29.72	36.90	17.76	51.26	12.67
25	43.32	46.32	57.54	27.64	79.98	19.69

Regarding the operating mode effect for classic needle-type applicators, the differences in temperature increments (ΔT) between the monopolar and bipolar modes are relatively marginal. At the maximum applied electrode voltage of 25 V, the ΔT-value for the monopolar applicator reached 46.32 °C, exceeding the result for the bipolar applicator ΔT = 43.32 °C by exactly 3 °C. This finding confirms stronger energy deposition at the single distal tip in a monopolar electrode configuration.

In contrast, the bipolar mode demonstrates a clear advantage in the case of expandable umbrella-type applicators. The bipolar configuration drastically amplifies the local temperature increment. For the 4-tine applicator at an electrode voltage of 25 V, the bipolar setup generated a temperature increment of 57.54 °C, whereas the monopolar setup achieved only ΔT = 27.64 °C, representing more than a twofold increase. Furthermore, analysis of the influence of the number of tines (four vs. eight) reveals inversion in RF applicator behavior. In the case of the bipolar mode, increasing the number of electrode arms (from four to eight) caused a substantial increase in ΔT (from 57.54 °C to 79.98 °C at 25 V) due to the densification of local current loops. Conversely, in the monopolar mode, adding four additional tines results in a notable decrease in the temperature increment (from 27.64 °C to 19.69 °C at 25 V). The expanded active surface area of the 8-tine umbrella-type applicator promotes stronger spatial dispersion of the electric current flowing toward the distant ground electrode, which ultimately lowers the ΔT value at the central measurement point of the hepatic tumor.

4. Discussion

To accurately assess the therapeutic efficacy of RF ablation treatment for all the analyzed applicator configurations, it is necessary to determine the volumes of the ablation zones and compare them with the volume of the ellipsoidal hepatic tumor under treatment.

In our case, it was assumed that 3D isothermal (ISO) surfaces allow precise characterization of the extent of thermal damage within the hepatic tumor. To visualize this effect, ISO surfaces within the tumor tissue for critical temperatures 43 °C, 53 °C, and 60 °C are depicted in Figure 9. The ablation zone volume progressively decreases as the required temperature threshold increases. While the ISO-43 surface defines the broad boundary of hyperthermia treatment, the ISO-60 isotherm reveals the rigorous, central zone of instantaneous and irreversible coagulation necrosis, which is crucial for complete tumor eradication during RF ablation treatment.

For objective quantification of the results, the tissue volumes enclosed by the respective ISO surfaces were determined for all the applicator configurations at a maximum applied electrode voltage of 25 V. To ensure a strictly standardized and direct comparison, these results were evaluated relative to a single constant volume of the modeled ellipsoidally

shaped liver tumor across all the tested electrodes. This relationship was expressed using the therapeutic efficacy index, calculated according to the following formula:

$$\eta_{\mathrm{ISO}-T} = \frac{V_{\mathrm{ISO}-T}}{V_{\mathrm{tumor}}} \times 100\% \tag{6}$$

where $T \in \{43, 53, 60\}$ °C represents the critical temperature threshold, $V_{\mathrm{ISO}-T}$ is the measured volume of the ablation zone bounded by the given ISO surface, and V_{tumor} corresponds to the initial hepatic tumor volume V_{tumor} = 1941.2 mm^3. All the obtained data are summarized in Table 5.

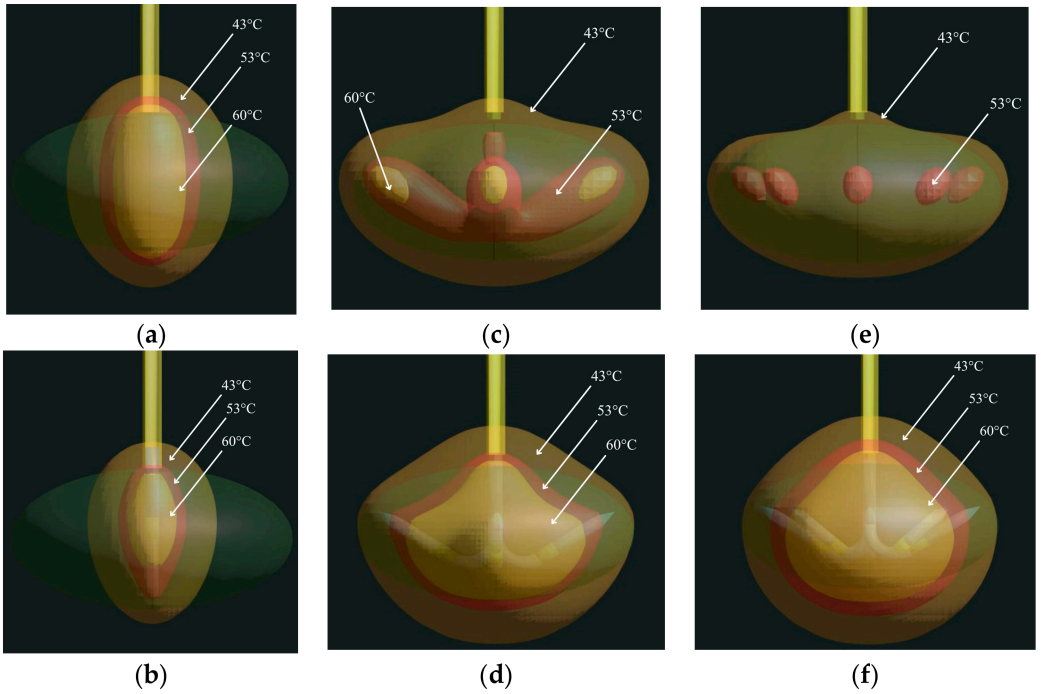


Figure 9. Spatial visualizations of the ISO surfaces inside the hepatic tumor tissue for various RF ablation applicator configurations: (**a**) monopolar needle-type applicator; (**b**) bipolar needle-type applicator; (**c**) monopolar expandable 4-tine umbrella-type applicator; (**d**) bipolar expandable 4-tine umbrella-type applicator; (**e**) monopolar expandable 8-tine umbrella-type applicator; (**f**) bipolar expandable 8-tine umbrella-type applicator; for applied electrode voltage of 25 V.

Table 5. A summary of the total ablation zone volumes for ISO surfaces at the critical temperatures of 43 °C, 53 °C, and 60 °C, and the therapeutic efficacy index after a 10 min RF ablation procedure for various applicators at an applied electrode voltage of 25 V.

Electrode Type	Tumor Volume V_{tumor} (mm^3)	Ablation Zone Volumes					
		$V_{\mathrm{ISO}-43}$ (mm^3)	$\eta_{\mathrm{ISO}-43}$ (%)	$V_{\mathrm{ISO}-53}$ (mm^3)	$\eta_{\mathrm{ISO}-53}$ (%)	$V_{\mathrm{ISO}-60}$ (mm^3)	$\eta_{\mathrm{ISO}-60}$ (%)
monopolar needle	1941.20	1059.94	58.4	347.04	18.5	170.41	9.0
bipolar needle		551.03	29.0	120.68	5.6	41.20	2.1
monopolar 4-tine umbrella		2536.84	130.7	340.47	17.5	24.59	1.3
bipolar 4-tine umbrella		2574.88	132.6	892.95	46.0	550.99	28.4
monopolar 8-tine umbrella		2409.33	124.1	51.05	2.6	0	0
bipolar 8-tine umbrella		3370.72	173.6	1544.94	79.6	926.92	47.7

A detailed analysis of the volumetric data for the considered ablation zones reveals fundamental differences in the behavior of individual RF applicators, resulting from the

mechanisms of electric field distribution inside hepatic tissue. For large tumors treated using expandable multi-tine umbrella-type applicators, the bipolar mode proved to be the most effective configuration in creating an ablation zone of immediate necrosis (ISO-60 zone). Closure of the electric current between the tines and shaft causes a strong concentration of heat. The 8-tine bipolar applicator achieved the largest ablation volume of 926.92 mm^3, corresponding to 47.7% coverage of the hepatic tumor volume. Reducing the number of tines to four in the bipolar umbrella-type applicator lowered this efficacy to 28.4% (550.99 mm^3). A particularly important physical phenomenon is the drastic drop in liver tumor coverage for multi-tine applicators operating in the monopolar mode. The four-tine monopolar applicator achieved only 1.3% tumor coverage (24.59 mm^3) for the rigorous 60 °C isotherm. The zero-volume value for the ISO-60 zone in the case of the eight-arm monopolar applicator results from the extreme dispersion of the electric field lines across a very large active surface area, thereby drastically reducing the local electric current density. Consequently, the system is unable to generate sufficient resistive heating to reach the critical necrosis threshold, and the maximum temperature recorded within the tumor volume reached only 53 °C. The failure to form a zone of immediate coagulation clearly demonstrates that, for multi-arm monopolar systems to operate effectively in large neoplastic lesions, it is essential to use significantly higher supply voltages.

An opposite trend was observed for classic needle-type applicators. Here, the monopolar configuration demonstrated a distinct advantage, generating an ISO-60 zone with a volume of 170.41 mm^3, corresponding to 9.0% coverage of the target tumor. The bipolar version of the same needle applicator achieved only 41.02 mm^3 (η_{ISO-60} = 2.1%). This phenomenon can be explained by the fact that around a single, monopolar active tip, the E-field propagates radially into deeper regions of the liver tissue. In the bipolar needle, RF field energy is largely confined in the dielectric gap of the insulator, failing to penetrate the peripheral regions of the large hepatic tumor. Furthermore, it can be noted that the efficacy coefficient η_{ISO-43} exceeded 100% for multi-tine applicators. This observation indicates that the ablation zone may extend beyond the tumor volume, which in turn may lead to damage to healthy tissue, which may compromise treatment precision and increase the risk of collateral tissue damage.

In conclusion, none of the analyzed single applicator configurations at the applied electrode voltage 25 V and treatment time of 600 s was able to generate an ISO-60 ablation zone covering the entire tumor volume.

For a more comprehensive assessment of the degree of hepatic tissue destruction, alongside the classic analysis of ISO surfaces, the cumulative equivalent minutes at 43 °C (CEM_{43}) thermal dose model was employed. This model allows quantitative determination of the cumulative heat dose absorbed by the liver tissue throughout the RF ablation procedure, integrating both the effect of the achieved temperature and the exposure time. The CEM_{43} index was calculated based on Equation (5), according to the widely accepted thermal dose model [17–19].

Figure 10 presents the spatial distributions of the determined CEM_{43} thermal dose index on axial cross-sections for all the tested applicator configurations. This analysis was performed for a 10 min ablation procedure at a constant applied electrode voltage of 25 V. The bright central regions (white zones on the scale) represent areas where the CEM_{43} index substantially exceeds the required threshold values. From a clinical perspective, these regions define the thermal zone of irreversible coagulation necrosis of the tumor cells.

The visualizations of CEM_{43} distributions fully confirm the physical mechanisms identified based on isothermal volume analysis. For the expandable multi-tine electrodes in the bipolar mode, a strong and highly localized accumulation of destructive thermal dose confined within the space between the tines and the shaft is evident. Changing to the

monopolar mode (for electrodes with both four and eight tines) results in the diffusion of the thermal damage zone and the absence of pronounced dose accumulation in the center of the hepatic tumor. Conversely, for classic needle-type electrodes, the effective thermal dose-zone region assumes the shape of an elongated ellipsoid. The results clearly show that around a single, monopolar tip, the destruction zone extends more deeply into the liver tissue, whereas in the bipolar needle, the CEM_{43} distribution remains confined to the area of the dielectric gap.

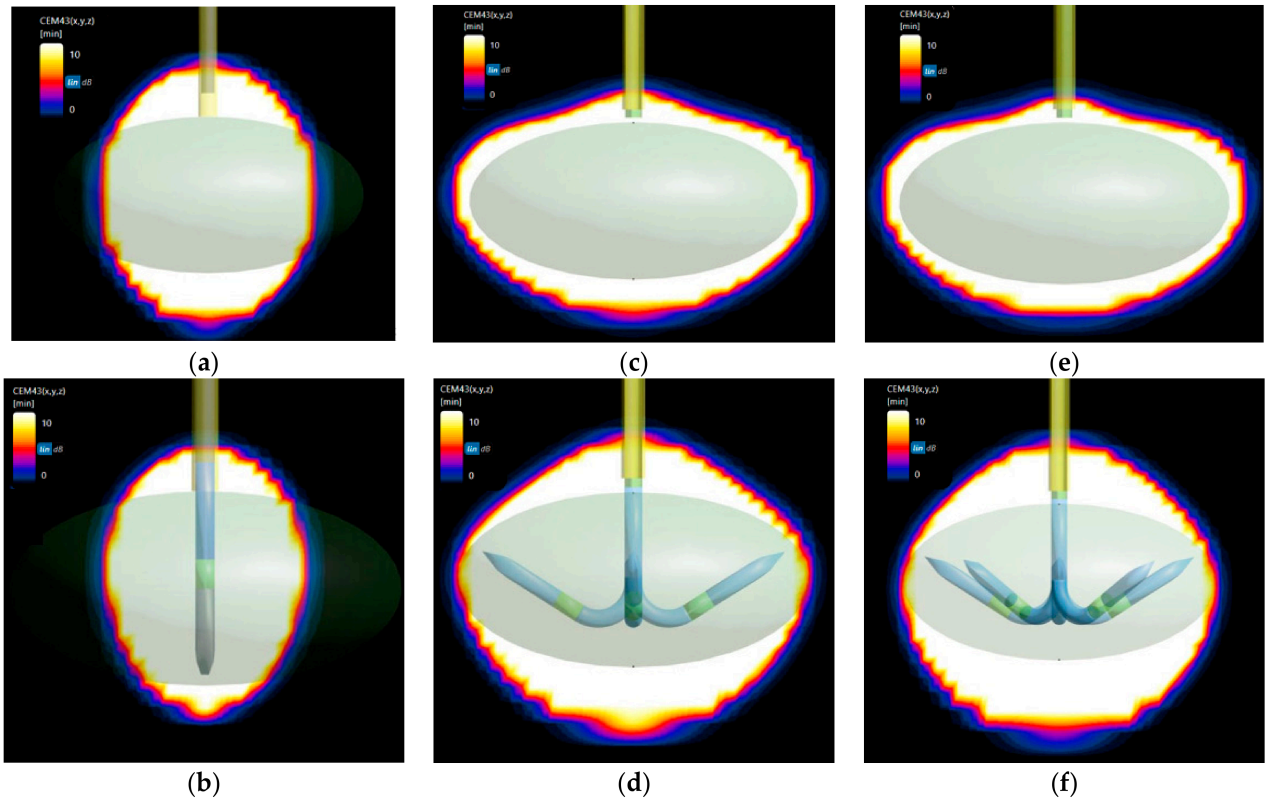


Figure 10. The spatial distributions of the CEM_{43} thermal dose index within the hepatic tumor model after a 10 min ablation procedure for various RF applicator configurations: (**a**) monopolar needle-type applicator; (**b**) bipolar needle-type applicator; (**c**) monopolar expandable 4-tine umbrella-type applicator; (**d**) bipolar expandable 4-tine umbrella-type applicator; (**e**) monopolar expandable 8-tine umbrella-type applicator; (**f**) bipolar expandable 8-tine umbrella-type applicator; for applied electrode voltage of 25 V. The bright, central zones indicate areas where the thermal dose threshold has been substantially exceeded, corresponding to the zone of irreversible coagulative necrosis of the tissue.

5. Conclusions

The numerical investigations conducted in this study enabled a detailed evaluation of RF thermal ablation efficacy in a liver tumor model using various RF applicator configurations. The results were obtained using a coupled electro-thermal mathematical model based on the generalized Laplace equation and the Pennes bioheat equation. The temperature distribution within a liver tumor model, the RF energy deposition within the tumor, and the heating dynamics of the tumor during a 10 min ablation procedure were investigated. Due to blood perfusion (the heat sink effect), transient liver tissue temperatures stabilized at steady-state values. To ensure consistency among the applicators, the Neumann boundary condition and temperature-independent dielectric properties were used in the temperature analysis. Although this modeling approach represents a limitation of the study, it remains

appropriate for a direct comparison of the applicators, which should remain independent of variations in the assumed material coefficients.

For standard needle-type applicators, the monopolar operating mode demonstrated a clear advantage. In this configuration, the electric field propagates radially from a single active tip deep into the hepatic tissue. This enables more effective and broader tumor coverage by the critical 60 °C ablation zone. In contrast, in the case of bipolar needle configuration, EM energy is strongly trapped in the dielectric gap between the poles. This confinement drastically limits the total volume of the necrosis zone, rendering the bipolar mode less effective for classic needle applicators.

A markedly different behavior was observed for large hepatic tumors treated with multi-tine expandable umbrella-type applicators. In this case, the bipolar mode led to highly localized concentration of RF field energy within the umbrella electrode. Although this generated the largest necrotic volume within the central region of the liver tumor (especially for the 8-tine applicator), the strong E-field confinement may result in insufficient heating of the peripheral tumor margins.

On the other hand, the application of the monopolar mode to multi-tine electrodes results in a substantial spatial dispersion of the electric current toward the distant grounding electrode. Consequently, at an applied electrode voltage of 25 V, the tissue did not reach the critical coagulative necrosis threshold of 60 °C. This proves that monopolar multi-tine applicator designs require substantially higher electric power inputs to be more effective.

Overall, the quantitative results demonstrate that none of the investigated RF applicator configurations, operating at an applied electrode voltage of 25 V during a 10 min ablation procedure, was able to generate an ablation zone covering 100% of the targeted liver tumor volume. The simulations presented in this study were conducted using a constant-voltage excitation model. In clinical practice, however, RF ablation systems typically use power-controlled or impedance-controlled feedback algorithms to dynamically regulate EM energy delivery in response to changes in tissue properties during heating. Consequently, the present model does not fully replicate the closed-loop control behavior of clinical RF generators. The constant-voltage framework was adopted to provide a consistent and computationally tractable framework for comparative evaluation of RF applicator performance and local electro-thermal interactions. Incorporating generator feedback control and temperature-dependent power regulation is an important step toward achieving greater clinical realism in future work. Furthermore, although the model captures the primary mechanisms governing temperature distribution, caution should be exercised when directly translating quantitative treatment metrics into clinical practice.

Author Contributions: Conceptualization, M.G., A.M. and P.G.; methodology, M.G., A.M. and P.G.; software, M.G.; validation, M.G., A.M. and P.G.; formal analysis, M.G., A.M. and P.G.; investigation, M.G., A.M. and P.G.; resources, M.G., A.M. and P.G.; data curation, M.G. and A.M.; writing—original draft preparation, M.G.; writing—review and editing, A.M. and P.G.; visualization, M.G.; supervision, A.M. and P.G.; project administration, A.M. and P.G.; funding acquisition, M.G., A.M. and P.G. All authors have read and agreed to the published version of the manuscript.

Funding: The work is the result of research funded by grant no. 16/PPL/2025/F 'Pearls of the Lublin University of Technology' as part of the 'Lublin University of Technology—Scientific Excellence' strategy. The work is also the result of research funded by grant no. 16.16.120.773 from the Ministry of Science and Higher Education for scientific activity conducted at the Department of Electrical and Power Engineering at the AGH University of Krakow.

Institutional Review Board Statement: Not applicable.

Informed Consent Statement: Not applicable.

Data Availability Statement: The data supporting the reported results can be obtained upon request from the corresponding authors.

Conflicts of Interest: The authors declare no conflicts of interest.

References

1. Jiang, Z.; Yang, F. New advances in the treatment of intermediate and advanced hepatocellular carcinoma. *Front. Oncol.* **2024**, *14*, 1430991. [CrossRef] [PubMed]
2. Seda, P.; Abbey, R.; Peng, L.; Ezeaku, I.; Laroia, S.T.; Aziz, H. A review of established and new developments in local therapies for liver cancer. *ESMO Gastrointest. Oncol.* **2026**, *11*, 100283. [CrossRef]
3. Komorowski, A.L. The Emerging Role of Ablation in the Treatment of Primary and Metastatic Cancer of the Liver. *J. Clin. Med.* **2025**, *14*, 8016. [CrossRef]
4. Asran, M.; Selim, M.F.; Ashour, A.S. Novel T-ring-based probes for thermal ablation of tumors in different organs. *Sci. Rep.* **2025**, *15*, 43251. [CrossRef]
5. Garcia, E.P.; Rubio, M.F.J.C.; Guerrero Lopez, G.D.; Felix, K.S.; Hernandez Jaquez, J.I.; Garcia, F.F.; Vera Hernandez, A.; Salas, L.L. Impact of Breast Tissue Heterogeneity on Microwave Ablation Performance: Insights from Computational Modeling. *Curr. Cancer Ther. Rev.* **2025**, *21*, 574–585. [CrossRef]
6. Zhang, H.; Qin, X.; Sun, Y.; Liu, Y. Electrodes of radiofrequency ablation for malignant lung tumors: A narrative review of advances, applications, and prospects. *J. Thorac. Dis.* **2026**, *18*, 253. [CrossRef]
7. Slusarczyk, A.; Gurwin, A.; Barnas, A.; Ismail, H.; Miszczyk, M.; Zapala, P.; Przydacz, M.; Krajewski, W.; Antczak, A.; Zyczkowski, M.; et al. Outcomes of focal therapy for localized prostate cancer: A systematic review and meta-analysis of prospective studies. *Eur. Urol. Oncol.* **2025**, *8*, 1653–1672. [CrossRef] [PubMed]
8. Szymanska, D.; Fusnik, L.; Miaskowski, A. Application of magnetic hyperthermia in prostate cancer treatment. *Acta Bioeng. Biomech.* **2026**, *28*, 17. [CrossRef]
9. Mulier, S.; Miao, Y.; Mulier, P.; Dupas, B.; Pereira, P.; de Baere, T.; Lencioni, R.; Leveillee, R.; Marchal, G.; Michel, L.; et al. Electrodes and multiple electrode systems for radiofrequency ablation: A proposal for updated terminology. *Eur. Radiol.* **2005**, *15*, 798–808. [CrossRef]
10. Razek, A. From Open, Laparoscopic, or Computerized Surgical Interventions to the Prospects of Image-Guided Involvement. *Appl. Sci.* **2025**, *15*, 4826. [CrossRef]
11. Bates, A.P.; Ullah, W. The Biophysics of Radiofrequency Ablation and Factors Affecting Lesion Size. *Arrhythm. Electrophysiol. Rev.* **2026**, *15*, e08. [CrossRef]
12. Ran, J.; Benedetti, E.; Bentsman, J.; Berlin, R.; Giulianotti, P.C.; Ostoja-Starzewski, M. Modeling of Radio Frequency Ablation and Electrosurgery: Capturing Tissue Carbonization and Stalling Phenomena. *J. Biomech. Eng.* **2026**, *148*, 041009. [CrossRef]
13. Strand, N.H.; Hagedorn, J.M.; Dunn, T.; Johnson, B.; Abd-Elsayed, A.; Covington, S.; Freeman, J.; Dawodu, A.; Maloney, J. Advances in radiofrequency ablation: Mechanism of action and technology. *Ann. Palliat. Med.* **2024**, *13*, 1028–1034. [CrossRef] [PubMed]
14. Gas, P.; Miaskowski, A. Influence of the radiofrequency applicators arrangement on the sizes of ablative zones inside hepatic tumor. *Arch. Electr. Eng.* **2024**, *73*, 557–571. [CrossRef]
15. Gas, P.; Kurgan, E. Evaluation of thermal damage of hepatic tissue during thermotherapy based on the Arrhenius model. In *Proceedings of the 2018 Progress in Applied Electrical Engineering (PAEE), Koscielisko, Poland, 18–22 June 2018*; IEEE: New York, NY, USA, 2018; pp. 1–4. [CrossRef]
16. Hamzavi, F.; Karimi, M.J.; Bahadoran, M. Numerical analysis of microwave and radiofrequency ablations: A novel design for electrode-based radiofrequency ablation. *J. Therm. Biol.* **2025**, *132*, 104247. [CrossRef]
17. van Rhoon, G.C. Is CEM43 still a relevant thermal dose parameter for hyperthermia treatment monitoring? *Int. J. Hyperth.* **2016**, *32*, 50–62. [CrossRef]
18. Geoghegan, R.; Ter Haar, G.; Nightingale, K.; Marks, L.; Natarajan, S. Methods of monitoring thermal ablation of soft tissue tumors–A comprehensive review. *Med. Phys.* **2022**, *49*, 769–791. [CrossRef] [PubMed]
19. Miaskowski, A. Temperature analysis in prostate tumor during radiofrequency ablation. *Prz. Elektrotechniczn.* **2025**, *101*, 251–256. [CrossRef]
20. Gas, P. Modelling the temperature-dependent RF ablation produced by the multi-tine electrode. *Prz. Elektrotechniczn.* **2020**, *96*, 48–51. [CrossRef]
21. Trujillo, M.; Berjano, E. Review of the mathematical functions used to model the temperature dependence of electrical and thermal conductivities of biological tissue in radiofrequency tumor ablation. *Int. J. Hyperth.* **2013**, *29*, 590–597. [CrossRef] [PubMed]
22. Haemmerich, D.; Webster, J.G. Automatic control of finite element models for temperature-controlled radiofrequency ablation. *BioMed. Eng. OnLine.* **2005**, *4*, 42. [CrossRef] [PubMed]

23. Lodato, F.; De Vita, E.; Patrone, R.; Izzo, F.; Iadicicco, A.; Campopiano, S.; Massa, R.; Riccio, D.; Ruello, G. Radio Frequency Ablation of Liver Tissue assisted by Saline Infusion: Computational Modeling and Experimental Assessment. *IEEE Trans. Instrum. Meas.* **2025**, *74*, 4008711. [CrossRef]
24. Pennes, H.H. Analysis of Tissue and Arterial Blood Temperatures in the Resting Human Forearm. *J. Appl. Physiol.* **1998**, *85*, 5–34. [CrossRef]
25. Singh, A.; Singh, H.; Kumar, N.; Safdari Shadloo, M. Estimation of the effect of blood vessels on magnetic hyperthermia therapy of liver tumors using patient-specific anatomical models. *Phys. Fluids.* **2025**, *37*, 091918. [CrossRef]
26. Nain, S.; Kumar, N.; Avti, P.K. Effect of arterial blood flow on magnetic nanoparticle thermotherapy applied on a realistic breast tumor model. *Int. J. Numer. Methods Biomed. Eng.* **2025**, *41*, e70039. [CrossRef] [PubMed]
27. Boregowda, G.; Mariappan, P. Effect of high blood flow on heat distribution and ablation zone during microwave ablation-numerical approach. *Int. J. Numer. Methods Biomed. Eng.* **2024**, *40*, e3835. [CrossRef]
28. Shu, S.; Yang, G.; Han, H.; Zhan, T.; Dang, H.; Xu, Y. Accurate temperature reconstruction in radiofrequency ablation for atherosclerotic plaques based on inverse heat transfer analysis. *J. Biomech. Eng.* **2024**, *146*, 081010. [CrossRef]
29. Fakhradini, S.S.; Mosharaf-Dehkordi, M.; Ahmadikia, H. Evaluating antenna configurations for improved microwave therapy outcomes in liver tumors enhanced with magnetic nanoparticles. *J. Therm. Biol.* **2025**, *135*, 104365. [CrossRef]
30. Kim, D.; Kim, H. Numerical Analysis of Therapeutic Effects by Varying Slot Numbers and Slot-to-Slot Distance in Microwave Ablation using Multislot Coaxial Antenna. *Int. J. RF Microw. Comput.-Aided Eng.* **2024**, *2024*, 8841831. [CrossRef]
31. Boskovic, N.; Radjenovic, B.; Radmilovic-Radjenovic, M. Optimal parameters for the efficient microwave ablation of liver tumor from the 3D-IRCADb-01 database. *Acta Bioeng. Biomech.* **2024**, *26*, 47–54. [CrossRef]
32. Hoffer, E.K.; Drinane, M.C.; Bhatnagar, V.; Mehta, R.; Munger, D.P.; Borsic, A. Radiofrequency ablation of hepatocellular carcinoma guided by real-time physics-based ablation simulation: A prospective study. *Int. J. Hyperth.* **2024**, *41*, 2331704. [CrossRef]
33. Soetaert, F.; Crevecoeur, G.; Dupre, L. Coupled electrical-thermal model for monopolar and bipolar radiofrequency liver tumor ablation. In Proceedings of the 2016 International Symposium on Fundamentals of Electrical Engineering (ISFEE), Bucharest, Romania, 30 June–2 July 2016; pp. 1–5. [CrossRef]
34. Wang, S.; Yao, Y.; Cui, H. Research progress on simulation of radiofrequency ablation for liver cancer treatment. *Prog. Med. Devices* **2025**, *3*, 96–105. [CrossRef]
35. Miaskowski, A.; Gas, P. Numerical Estimation of SAR and Temperature Distributions inside Differently Shaped Female Breast Tumors during Radio-Frequency Ablation. *Materials* **2023**, *16*, 223. [CrossRef]
36. Gupta, P.R.; Ghosh, P. Assessing the Thermal Damage Induced by Radiofrequency Ablation for Localized Liver Cancer. *ASME J. Heat Mass Transf.* **2025**, *147*, 011201. [CrossRef]
37. Michalowska-Samonek, J.; Miaskowski, A.; Wac-Wlodarczyk, A. Numerical analysis of high frequency electromagnetic field distribution and specific absorption rate in realistic breast models. *Prz. Elektrotechniczn.* **2012**, *88*, 97–99.
38. Szczech, M.; Sikora, W. The influence of printing parameters on leakage and strength of fused deposition modelling 3D printed parts. *Adv. Sci. Technol. Res. J.* **2024**, *18*, 195–201. [CrossRef]
39. Wang, Q.; Wu, S.; Li, L.; Xue, X.; Zhang, H.; Wu, W.; Gao, H. Personalized Simulation Modeling of Overlapping Microwave Ablation for Large Tumors. *Bioengineering* **2026**, *13*, 421. [CrossRef] [PubMed]
40. Suleman, M.; Mehmood, A.; Khan, S.U.; Abdullah, N.; Aoudia, M.; Maatki, C.; Kolsi, L. Advanced finite element simulations for brain tumor hyperthermia using polycrystalline Fe3O4 superparticles with optimized thermal radiation control. *J. Radiat. Res. Appl. Sci.* **2025**, *18*, 101916. [CrossRef]
41. *Sim4Life Lite*, version 9.4.0; Zurich MedTech AG: Zurich, Switzerland, 2026. Available online: https://s4l-lite.io/ (accessed on 15 April 2026).
42. *Sim4Life Web Lite Documentation*, 2.7.1 EM LF Simulation Theory; Zurich MedTech AG: Zurich, Switzerland, 2024. Available online: https://sim4life.swiss (accessed on 15 April 2026).
43. Cheng, D.K. *Fundamentals of Engineering Electromagnetics*; Pearson New International Edition; Pearson: London, UK, 2013.
44. Paruch, M. Sensitivity analysis and the inverse problem in the mathematical modelling of tumor ablation using the interstitial hyperthermia. *AIP Conf. Proc.* **2020**, *2239*, 020038. [CrossRef]
45. Gaugain, G.; Queguiner, L.; Bikson, M.; Sauleau, R.; Zhadobov, M.; Modolo, J.; Nikolayev, D. Quasi-static approximation error of electric field analysis for transcranial current stimulation. *J. Neural Eng.* **2023**, *20*, 016027. [CrossRef]
46. Syrek, P.; Skowron, M.; Kapustka, P. Eddy Current Distribution in Magnetotherapy of Bones: A Qualitative and Quantitative Study. *Appl. Sci.* **2025**, *15*, 9892. [CrossRef]
47. Tucci, C.; Trujillo, M.; Berjano, E.; Iasiello, M.; Andreozzi, A.; Vanoli, G.P. Pennes' bioheat equation vs. porous media approach in computer modeling of radiofrequency tumor ablation. *Sci. Rep.* **2021**, *11*, 5272. [CrossRef] [PubMed]
48. Alamouti, A.K. Dynamic physiological and structural tissue parameters in bioheat models: Enhancing heat transfer realism for hyperthermia therapy. *Int. Commun. Heat Mass Transf.* **2026**, *175*, 111185. [CrossRef]

49. Ahamed, K.P.S.; Arunachalam, K. Multifrequency operation of an intracavitary monopole with sliding broadband choke for delivering hyperthermia treatment with variable coverage. *Electromagn. Biol. Med.* **2024**, *43*, 256–266. [CrossRef]
50. Kumar, D.; Ansari, F.; Singh, J. Computational analysis of nonlinear bioheat transfer equation of multilayered brain tissue with porosity during tumor thermal therapy. *Eur. Phys. J. Plus.* **2026**, *141*, 437. [CrossRef]
51. Imanlou, S.; Vafai, K. Analysis of magnetothermal hyperthermia on tumor ablation and Parkinson's therapy. *Int. J. Heat Mass Transf.* **2026**, *254*, 127697. [CrossRef]
52. Baumgartner, C.; Hasgall, P.A.; Di Gennaro, F.; Neufeld, E.; Lloyd, B.; Gosselin, M.C.; Payne, D.; Klingenbock, A.; Kuster, N. IT'IS Database for Thermal and Electromagnetic Parameters of Biological Tissues, Version 5.0. 21 August 2025. Available online: https://itis.swiss/virtual-population/tissue-properties/ (accessed on 15 April 2026).
53. Ansari, F.; Singh, J. Bioheat transfer analysis inside multi-layered breast tissue during magnetic hyperthermia: Incorporating sweating and surface heat sources. *Int. Commun. Heat Mass Transf.* **2025**, *168*, 109365. [CrossRef]
54. Mouratidis, P.X.; Rivens, I.; Civale, J.; Symonds-Tayler, R.; Ter Haar, G. Relationship between thermal dose and cell death for "rapid" ablative and "slow" hyperthermic heating. *Int. J. Hyperth.* **2019**, *36*, 228–242. [CrossRef]
55. Dewhirst, M.; Viglianti, B.L.; Lora-Michiels, M.; Hoopes, P.J.; Hanson, M.A. Thermal dose requirement for tissue effect: Experimental and clinical findings. In *Thermal Treatment of Tissue: Energy Delivery and Assessment II*; SPIE: Bellingham, WA, USA, 2003; Volume 4954, pp. 37–57. [CrossRef]
56. Sapareto, S.A.; Dewey, W.C. Thermal dose determination in cancer therapy. *Int. J. Radiat. Oncol. Biol. Phys.* **1984**, *10*, 787–800. [CrossRef]
57. STARmed Co., Ltd. Ablation Size Data (Bovine Ex-Vivo Test), ST-SD-06 Rev.1, Goyang-si, Gyeonggi-do, Korea. 2022. Available online: www.STARmed4u.com (accessed on 15 April 2026).
58. Dolciotti, N.; D'Agostino, S.; Colella, M.; Apollonio, F.; Liberti, M. Advances in Female Chest Modeling: Enhanced 3D Dosimetric Models Across Two Illustrative Scenarios. *Bioelectromagnetics* **2025**, *46*, e70034. [CrossRef]

Disclaimer/Publisher's Note: The statements, opinions and data contained in all publications are solely those of the individual author(s) and contributor(s) and not of MDPI and/or the editor(s). MDPI and/or the editor(s) disclaim responsibility for any injury to people or property resulting from any ideas, methods, instructions or products referred to in the content.